Check for updates

ADVANCED MATERIALS
www.advmat.de

Improving OFF-State Bias-Stress Stability in High-Mobility Conjugated Polymer Transistors with an Antisolvent Treatment

*Malgorzata Nguyen, Ulrike Kraft, Wen Liang Tan, Illia Dobryden, Katharina Broch, Weimin Zhang, Hio-Ieng Un, Dimitrios Simatos, Deepak Venkateshavaran, Iain McCulloch, Per M. Claesson, Christopher R. McNeill, and Henning Sirringhaus**

Conjugated polymer field-effect transistors are emerging as an enabling technology for flexible electronics due to their excellent mechanical properties combined with sufficiently high charge-carrier mobilities and compatibility with large-area, low-temperature processing. However, their electrical stability remains a concern. ON-state (accumulation mode) bias-stress instabilities in organic semiconductors have been widely studied, and multiple mitigation strategies have been suggested. In contrast, OFF-state (depletion mode) bias-stress instabilities remain poorly understood despite being crucial for many applications in which the transistors are held in their OFF-state for most of the time. Here, a simple method of using an antisolvent treatment is presented to achieve significant improvements in OFF-state bias-stress and environmental stability as well as general device performance for one of the best performing polymers, solution-processable indacenodithiophene-*co*-benzothiadiazole (IDT-BT). IDT-BT is weakly crystalline, and the notable improvements to an antisolvent-induced, increased degree of crystallinity, resulting in a lower probability of electron trapping and the removal of charge traps is attributed. The work highlights the importance of the microstructure in weakly crystalline polymer films and offers a simple processing strategy for achieving the reliability required for applications in flexible electronics.

1. Introduction

In the last ten years, organic semiconductor (OSC) mobilities >1–10 $cm^2\ V^{-1}\ s^{-1}$ have been reported for both small molecules and polymeric thin films,[1–4] exceeding the benchmark of amorphous silicon (0.5–1 $cm^2\ V^{-1}\ s^{-1}$).[5,6] With these advances, organic field-effect transistors (OFETs) have evolved from a convenient tool for quantifying material performance to an emerging large-area technology entering the market as circuit components driving flexible electronics such as wearables, active-matrix displays, sensor arrays, and bioelectronics.[7–9]

One of the remaining bottlenecks in the progress of OFETs toward becoming a ubiquitous technology is a lack of understanding of the factors that govern their environmental, thermal, and operational

M. Nguyen, H.-I. Un, D. Simatos, D. Venkateshavaran, H. Sirringhaus
Optoelectronics Group
Cavendish Laboratory
University of Cambridge
J.J. Thomson Avenue, Cambridge CB3 0HE, UK
E-mail: hs220@cam.ac.uk

U. Kraft
Max Planck Institute for Polymer Research
PI-P, Ackermannweg 10, 55128 Mainz, Germany

W. L. Tan, C. R. McNeill
Department of Material Science and Engineering
Monash University
Wellington Rd, Clayton, Victoria 3800, Australia

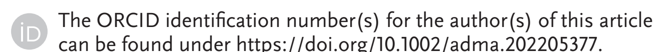
The ORCID identification number(s) for the author(s) of this article can be found under https://doi.org/10.1002/adma.202205377.

© 2023 The Authors. Advanced Materials published by Wiley-VCH GmbH. This is an open access article under the terms of the Creative Commons Attribution License, which permits use, distribution and reproduction in any medium, provided the original work is properly cited.

DOI: 10.1002/adma.202205377

I. Dobryden, P. M. Claesson
KTH Royal Institute of Technology
School of Engineering Sciences in Chemistry, Biotechnology and Health
Department of Chemistry
Division of Surface and Corrosion Science
Drottning Kristinas väg 51, SE-100 44 Stockholm, Sweden

I. Dobryden
Experimental Physics
Division of Materials Science
Department of Engineering Sciences and Mathematics
Luleå University of Technology
SE-971 87 Luleå, Sweden

K. Broch
Institut für Angewandte Physik
University of Tübingen
Geschwister-Scholl-Platz, 72074 Tübingen, Germany

W. Zhang, I. McCulloch
Physical Science and Engineering Division
King Abdullah University of Science and Technology
King Abdullah University of Science and Technology
4700 KAUST, Thuwal 23955-6900, Kingdom of Saudi Arabia

I. McCulloch
Department of Chemistry
University of Oxford
Mansfield Rd, Oxford OX1 3TA, UK

15214095, 2023, 16, Downloaded from https://onlinelibrary.wiley.com/doi/10.1002/adma.202205377 by MPI 355 Polymer Research, Wiley Online Library on [10/07/2023]. See the Terms and Conditions (https://onlinelibrary.wiley.com/terms-and-conditions) on Wiley Online Library for rules of use; OA articles are governed by the applicable Creative Commons License

stabilities, which can result in unstable performance over time.[10] These instabilities manifest themselves as shifts in threshold voltage (V_{Th}), changes in mobility (μ) and ON/OFF current ratio, an increase in subthreshold swing (S), and an increased hysteresis in transfer characteristics of a device during operation.[5,8] Consequently, OFET-based sensors can yield erroneous extractions of measured quantities, decreased ON current results in an unstable pixel brightness in OFET-driven organic light-emitting diode (OLED) displays, while in OFET-driven organic liquid crystal displays (OLCDs), pixels can fail to switch properly due to a V_{Th} shift.[5,10] It is sometimes possible to overcome the V_{Th} instabilities through circuit compensation; nonetheless, it makes the devices significantly more complex.[11]

Trapping of mobile charge carriers due to conformational defects,[12,13] material impurities[14] or water-induced trap states,[15–17] either in the semiconductor or the gate dielectric, are the main reasons behind ON current degradation in OFETs. The formation of electronic states in the bandgap of the OSC leads to the accumulation of immobilized charges in the OSC, the dielectric, or the interface between the two, which reduces the mobility and creates trapped charge density that screens the conductive channel from the applied gate voltage.[18,19] Proposed mechanisms include a charge transfer across the semiconductor–dielectric interface[20] or electrochemical processes that lead to the formation of protons and their diffusion into the gate dielectric,[21] where they are subsequently trapped.

Bias-stress instabilities are observed when these charge trapping events occur due to the application of a prolonged bias to either the gate electrode or the drain electrode, or both. Significant effort has been directed at developing mitigation strategies for ON-state bias-stress instabilities, i.e., when the device is kept in the accumulation mode. One effective strategy has been the addition of small molecular additives to a *p*-type polymer semiconductor film.[22] These additives include *p*-type dopants,[23] electron-acceptors,[24] neutral molecular additives, and residual solvent molecules.[22]

However, these molecular additives do not have the same beneficial influence on the OFF-state bias-stress stability of OFETs that they do on ON-state stability.[25] This suggests that ON-state and OFF-state bias-stress instabilities require different mitigation strategies. Overall, the literature on improving OFF-state bias-stress stability of organic materials is scarce at best, even though it is an equally important issue. When used to drive capacitive display elements such as liquid crystal or electronic paper cells, OFETs stay in the depletion mode for most of the display addressing cycle and are only switched on for a short time interval to update the voltage held on the pixel. Excellent OFF-state stability is crucial for such switch-based applications of transistors, in which they are active only for short periods.[26]

Here, we present a simple but powerful method for improving OFF-state bias-stress stability and key device parameters, such as ON current, saturation mobility, and threshold voltage, in solution-processed OFETs made with a weakly crystalline polymer indacenodithiophene-*co*-benzothiadiazole (IDT-BT). The method involves treating the film using an orthogonal antisolvent, i.e., a solvent in which IDT-BT does not dissolve. We show that short exposure of a semiconductor film to orthogonal solvents results in a fourfold decrease in V_{Th} shift as well as better air stability and OFF-state bias-stress stability under light exposure. We observe an increased degree of crystallinity and polymer aggregation and propose a mechanism for the improved stability.

2. Electrical OFET Characterization

We chose IDT-BT with $C_{16}H_{33}$ side chains (shown in **Figure 1**a) for our studies due to its unprecedented high performance, with reports on mobility of >1 cm^2 V^{-1} s^{-1}[27] and low energetic disorder.[28] We used a top-gate-bottom-contact (TGBC) OFET architecture (shown in Figure 1b) because the staggered configuration of the gate and the source-drain contacts allows for more efficient charge injection.[29] A hydrophobic fluorinated dielectric Cytop with $\varepsilon = 2.1$ was used to minimize water-related traps at the semiconductor–dielectric interface and within the gate dielectric.[30,31]

The antisolvent treatment is an additional fabrication step after spin-coating of the IDT-BT film and involves the exposure of a wet IDT-BT film (spun from *o*-dichlorobenzene) to an excess of orthogonal solvent for 2 min, followed by an annealing step at 90 °C for 60 min to ensure solvent removal. We opted for this relatively low annealing temperature due to device performance being optimum near this temperature. When the devices were annealed at a higher temperature we observed a drop in performance, most likely due to increased contact resistance[32] (Figure S1, Supporting Information). Annealing at 90 °C is also compatible with the use of flexible substrates. Inspired by the work by Nikolka et al., which showed improved ON-state device performance after treatment with a variety of orthogonal solvents[33] but did not investigate OFF-state stability, we chose the two best-performing ones, i.e., acetonitrile and *n*-butyl acetate.

The treated devices exhibit a decrease in V_{Th} of 7.7 and 10.3 V (for acetonitrile and *n*-butyl acetate-treated devices, respectively) and an increased ON current in the transfer curve (Figure 1c) compared to untreated reference devices. They also exhibit a slightly steeper turn-on, with S = 4.3 and 4.8 V dec^{-1} for acetonitrile and *n*-butyl-acetate, respectively, compared to 5.1 V dec^{-1} for the reference, whereas their OFF currents are slightly elevated compared to the reference. Nonetheless, the output curves (Figure 1d) show a higher and more textbook-like linear regime of device operation, whereas the extracted mobility agrees with previous literature,[28,34] reaching values on the order of 1–2 cm^2 V^{-1} s^{-1}. Interestingly, the linear (μ_{lin}) and saturation (μ_{sat}) mobilities in both antisolvent-treated devices exhibit a less pronounced gate voltage dependence, reaching higher mobility values at lower gate voltages than the reference device and indicating more ideal transistor characteristics (Figure 1e). The higher mobility extracted in the saturation regime for the reference device is believed to be an artifact of the mobility extraction method.[32] Acetonitrile-treated devices exhibit a less negative threshold voltage and slightly higher linear and saturation mobility than the *n*-butyl-acetate-treated devices. The antisolvent-treated devices exhibit an unequivocal improvement across a number of parameters compared to the reference device.

© 2023 The Authors. Advanced Materials published by Wiley-VCH GmbH

15214095, 2023, 16, Downloaded from https://onlinelibrary.wiley.com/doi/10.1002/adma.202205377 by MPI 355 Polymer Research, Wiley Online Library on [10/07/2023]. See the Terms and Conditions (https://onlinelibrary.wiley.com/terms-and-conditions) on Wiley Online Library for rules of use; OA articles are governed by the applicable Creative Commons License

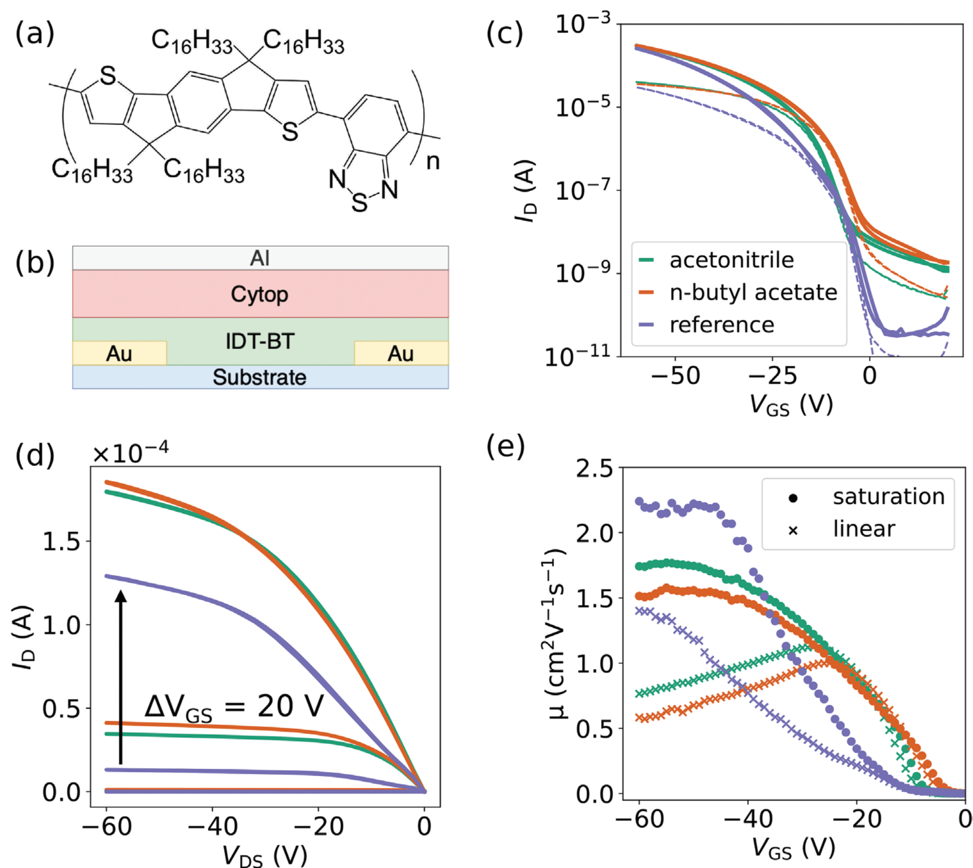

Figure 1. Electrical characterization of the acetonitrile- and *n*-butyl-acetate-treated IDT-BT OFETs compared with the reference. a) The chemical structure of IDT-BT. b) Schematic illustration of the TGBC OFET architecture used in this study with Ti/Au contact electrodes, IDT-BT organic layer, Cytop dielectric, and Al gate electrode. c) Saturation (V_{DS} = −60 V, solid line) and linear (V_{DS} = −5 V, dashed line) transfer characteristics of the devices. d) Output curves measured at V_{GS} = −10, −30, and −50 V. e) Gate voltage dependence of the saturation (dots) and linear mobilities (crosses).

3. Bias Stress Stability

When quantifying the accumulation stress stability, two common approaches are to measure either 1) the ON-state drain current under continuous bias stress or 2) the change in transfer curve characteristics as a function of stress time.[5] In both cases, constant gate voltage V_{GS} (and, optionally, a constant drain voltage V_{DS}) is applied to the device. Hence, the first method allows for continuous measurement, whereas the second method requires the interruption of the applied bias to obtain the transfer characteristics. Due to its nature, in the case of the depletion stress, we are limited to the latter approach, which runs a risk of shallow traps missing from the analysis caused by potential de-trapping when the bias stress is removed and a transfer curve is measured. However, this method gives valuable insight into the nature of the instability, allowing to extract the change in mobility, threshold voltage, subthreshold slope, and OFF-state current under bias stress.

The OFETs were subjected to a continuous bias of V_{DS} = −5 and V_{GS} = 50 V under an N_2 atmosphere (H_2O < 5 and O_2 < 5 ppm) and ambient yellow light for over 10 h, followed by a period of recovery when the bias was removed from the devices. The stress was also periodically removed for short periods to perform transfer curve measurements. The antisolvent-treated OFETs exhibited superior stability under these conditions, as shown in **Figures** 2a–c. The V_{Th} shift was just <1 V after a ten-hour stress period for both of the treated devices, which is over four times smaller than in the case of the reference device. Similar to the antisolvent-treated devices, the change in the ON-state current was on the scale of 3–4% (6–7 times smaller than reference), whereas the change in μ_{sat} was on the scale of 0–3% (compared to over 10% for the reference). Interestingly, the antisolvent-treated devices exhibited a fast and complete V_{Th} and mobility recovery, whereas the recovery in the untreated sample was incomplete, and degraded V_{Th} and μ_{sat} remained after a recovery period of several hours.

The time-dependence of bias stress instabilities is often modeled using a stretched exponential function that was first suggested to describe the threshold-voltage instabilities under stress in amorphous silicon transistors;[30,35]

$$\Delta V_{Th}(t) = \left(V_{Th}(\infty) - V_{Th}(0)\right)\left(1 - e^{-\left(\frac{t}{\tau}\right)^{\beta}}\right) \quad (1)$$

where $V_{Th}(0)$ is V_{Th} at t = 0, $V_{Th}(\infty)$ is V_{Th} at $t = \infty$ when equilibrium has been achieved, τ is the trapping time constant,

© 2023 The Authors. Advanced Materials published by Wiley-VCH GmbH

15214095, 2023, 16, Downloaded from https://onlinelibrary.wiley.com/doi/10.1002/adma.202205377 by MPI 355 Polymer Research, Wiley Online Library on [10/07/2023]. See the Terms and Conditions (https://onlinelibrary.wiley.com/terms-and-conditions) on Wiley Online Library for rules of use; OA articles are governed by the applicable Creative Commons License

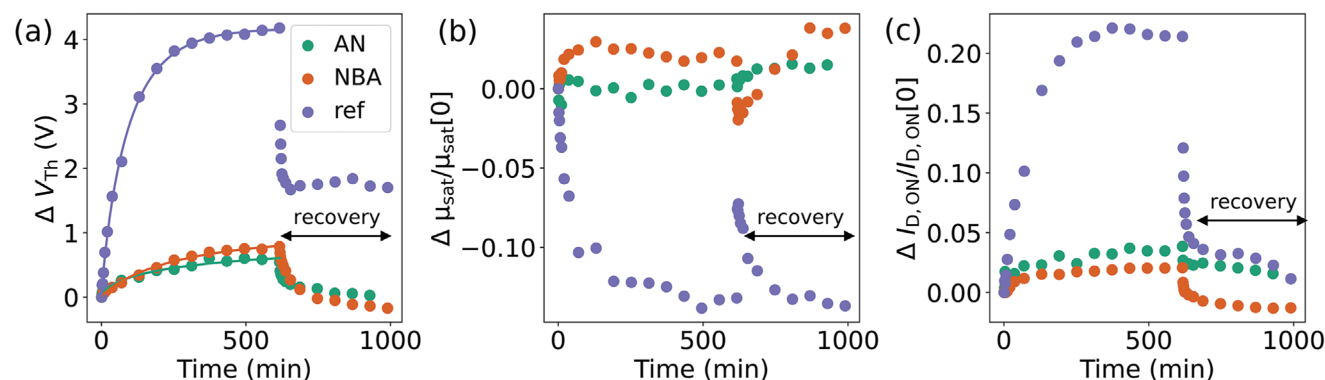

Figure 2. Change of the device parameters of the acetonitrile (AN) and *n*-butyl acetate (NBA) treated devices compared to the reference (ref) under prolonged OFF-state-bias stress at $V_{GS} = 50$ and $V_{DS} = -5$ V, where the continuous bias stress is stopped periodically to measure transfer characteristics. The recovery marked on the graphs corresponds to no voltage being applied between the electrodes. a) V_{Th} shift calculated from the saturation regime and the stretched exponential fit according to Equation 1. b) Change in saturation mobility μ_{sat} compared to μ_{sat} at $t = 0$ evaluated at $V_{GS} = -55$ V. c) Change of the ON current ($I_{D,ON}$) relative to $I_{D,ON}$ at $t = 0$.

and $\beta = T/T_0$ (where $0 < \beta \leq 1$) is the dispersion parameter. The stretched exponential function is applicable to dispersive processes in which there is a distribution of local environments[36] (such as trapping energies) that give rise to a distribution of τ, with β indicating the degree of variation of τ ($\beta = 1$ describes the exponential function with a singular τ).[37] **Table 1** shows extracted values of τ, β, and $\Delta V_{Th}(\infty)$. It highlights that $\Delta V_{Th}(\infty)$ is over four times higher and τ is over 2.5 times higher for both antisolvent treated devices compared to the reference. A larger trapping constant indicates that either the mean barrier height for charge trapping is higher or that the density of trap states is lower.

We thoroughly studied the source of the increased OFF current in the acetonitrile-treated device. One potential source is impurities contained in the acetonitrile doping the polymer film. To minimize this we used acetonitrile of the highest purity (see Experimental Section). We excluded the possibility of uncontrolled contaminant introduction during processing by performing the acetonitrile treatment under a purging N_2 atmosphere and using a new bottle of high-purity solvent. Next, we investigated the possibility of introducing oxygen during the antisolvent treatment that could potentially dope the polymer. Since both *n*-butyl acetate and acetonitrile are polar solvents, oxygen could diffuse through the suba-seal septa during solvent storage and dissolve into the solvents, even in high-purity assays. To exclude this as the contributing factor to the increased OFF current, we compared the device performance of OFETs in which the OSC layer was treated with the regular high-purity acetonitrile before and after one hour of solvent degassing with N_2. We did not observe a significant difference

Table 1. Trapping time constant τ, dispersion parameter β, and ΔV_{Th} at $t = \infty$ obtained by fitting Equation 1 to threshold-voltage shift plot shown in Figure 2a.

	τ [s^{-1}]	β	$\Delta V_{Th}[\infty]$ [V]
acetonitrile	2.63×10^4	0.55	0.87
n-butyl acetate	1.69×10^4	0.84	0.93
reference	5.66×10^3	0.88	4.18

in OFF currents of devices in which the OSC layer was treated with de-oxygenated and as-is acetonitrile (Figure S2, Supporting Information). Another common origin of high OFF currents in OFETs is the formation of a backchannel at the OSC-substrate interface. Glass substrates can be a source of ionic impurities that can diffuse into the film and affect the active channel formation during the transistor operation.[38] When using silicon oxide as the substrate (Figure S3, Supporting Information), we observed low OFF currents for both the reference and the acetonitrile-treated devices, while acetonitrile retained its beneficial effect on device performance and stability. OFF-state bias-stress measurements revealed that the beneficial effect of the antisolvent treatment on the OFF-state bias-stress stability remains regardless of the magnitude of the OFF current. This suggests that the enhanced OFF current observed after acetonitrile treatment is not linked to the improved bias stress and can be solved by the suitable substrate choice.

The pronounced improvement of OFF-state bias stability in the antisolvent-treated devices is consistently observed. The reproducibility of the result was ensured by averaging over six experiments, which is shown in Figure S4 (Supporting Information). We also investigated how the effectiveness of the treatment depends on the process conditions. We studied, for example, the influence of the time between the polymer deposition and the antisolvent treatment on the OFF-state stability of OFETs (shown in Figure S5, Supporting Information). The results show that performing the treatment straight away after semiconductor spin-coating yields devices with improved OFF-state bias-stress stability (reflected in threshold voltage, ON current, and mobility) compared to performing the treatment 2 min after semiconductor spin-coating. We attribute this effect to the fast evaporation of the solvent residues from the polymer film within the first 2 min, leaving the film drier, which prevents easy antisolvent distribution within the film. It is worth mentioning that this susceptibility to the timing of the antisolvent deposition contributes to a possible sample-to-sample variation in the treated devices that is reflected in Figure S4 (Supporting Information).

We removed the residual antisolvent after the treatment by annealing our devices for one hour at temperatures above

© 2023 The Authors. Advanced Materials published by Wiley-VCH GmbH

the boiling point of the antisolvents. We further investigated the effect of the residual solvents on the OFF-state bias-stress stability by intentionally leaving both the solvent (*o*-dichlorobenzene) and the antisolvent (acetonitrile) in the film, which was done by minimizing the annealing time of the OSC film to a few seconds only. We show that OFETs containing residues of either solvent exhibit 2 to 9 times higher V_{Th} shift under OFF-state bias-stress conditions applied for ten hours (Figure S6, Supporting Information). Moreover, the antisolvent treatment adopted in this work does not improve ON-current constant-voltage bias stress stability under $V_{GS} = -50$ for 10 h (Figure S7, Supporting Information). These results suggest that the mechanism involved in improving OFF-state stability is not related to the solvent-induced ON-state stability improvement caused by physical void filling that prevents water-related-trap formation, earlier reported by Nikolka et. al.[22]

To demonstrate the generality of our treatment to other semiconducting polymers, we applied the acetonitrile treatment to poly[[2,5-bis(2-octadecyl)-2,3,5,6-tetrahydro-3,6-diketopyrrolo[3,4-c]pyrrole-1,4-diyl]-*alt*-(2-octylnonyl)-2,1,3-benzotriazole] (DPP-BTz) (Figure S8, Supporting Information), a diketopyrrolopyrrole (DPP) based copolymer with mobilities exceeding 1 $cm^2\ V^{-1}\ s^{-1}$[39] and a more semicrystalline microstructure than IDT-BT.[40] In the device characteristics, we observe a similar increase in the current and lower dependence of mobility on the applied gate voltage. When the devices were subjected to ten hours of OFF-state bias stress at $V_{GS} = 50$ and $V_{DS} = -5$ V, the acetonitrile treatment improved the device stability, demonstrated by a three-times decrease in threshold-voltage shift, six-times decrease in ON current degradation and over two-times decrease in mobility degradation. This result demonstrates some level of generality of the treatment not only for the antisolvents used but also for different conjugated polymers.

Figure 3 shows temperature-dependent transfer curves and OFF-state bias-stress measurements on the reference and acetonitrile-treated devices between 220 and 320 K. The temperature dependence of the charge-carrier mobility gives insight into the transport mechanism of a given material and can provide information on the nature of the trap states involved. In Figure 3a, we observe a stronger temperature dependence of the transfer curves and an emergence of a larger hysteresis in the saturation regime of the reference devices (highlighted in Figure S9, Supporting Information) with a lower current measured in the reverse scan. This is consistent with the improved ON-state and sharper turn-on characteristics of the antisolvent-treated devices and indicates clearly that the treatment can suppress shallow hole trapping in the device. At the same time, the OFF current of the reference is more temperature-stable with only a 2.5 times increase between 320 and 200 K compared to a 20-times decrease in the case of the acetonitrile-treated device (Figure S10, Supporting Information).

The acetonitrile-treated devices are more stable under OFF-state bias stress and exhibit a lower V_{Th} shift after 3600 s across the entire range of investigated temperatures (Figure 3b). Figure 3c shows the temperature dependence of the threshold-voltage shift extracted at 3600 s. Within the measured temperature range, we distinguish a single $E_a = 81.9$ meV for the OFF-state bias stress of the reference and two $E_a = 68.2$ and $E_a = 202$ meV at $T < 280$ K and $T > 280$ K for the OFF-state bias stress of the antisolvent-treated device. Similar behavior is seen in the $V_{Th}(\infty)$ values extracted from stretched exponential fits (Figure S11, Supporting Information). These results suggest that there are at least two trapping mechanisms present in the acetonitrile-treated device and that the treatment results in one of these mechanisms effectively becoming suppressed below the freezing point of water. Therefore, we hypothesize that some of the residual trapping mechanism in the antisolvent treated devices may be water-related, which could indicate that during the treatment with the hygroscopic antisolvent additional water molecules are introduced into the film. This is unlikely to be beneficial, but at least it happens only to a limited degree, so that the overall effect of the treatment is a suppression the bias stress. We note that, in contrast to Kettner's results,[15] the bias stress is not fully suppressed at temperatures below the freezing point of water, with threshold-voltage shifts over 0.1 (antisolvent treatment) and 0.5 V (reference) after 3600 s remaining at 200–220 K.

4. Morphology and Microstructure

To investigate the origin of the significant improvement of the OFF-state bias stability achieved by our simple antisolvent treatment, we examined the morphological and crystallographic differences between the two films. We focused on the acetonitrile treatment due to its slightly better general performance and bias-stress stability. We conducted intermodulation atomic force microscopy (ImAFM) in the air on IDT-BT films prepared on glass, under identical fabrication conditions to the films in the transistor devices. The topographical images (**Figure 4**a,d,g) show a significantly increased roughness of the treated films with root-mean-square (RMS) of 8 nm, compared to 0.32 nm for the reference sample, and the distance from the peak to trough in the treated film with a thickness of 60 nm equal to 39.3 ± 3.3 nm. These are caused by solvent-induced swelling of the film, commonly observed in solvent-vapor annealing processes, where films are kept in solvent-rich atmospheres.[41,42] The trend of significantly increased roughness is also confirmed for a larger studied area of 4 µm × 4 µm, where the roughness increased from 0.42 nm for pristine IDT-BT to 7.3 nm for the acetonitrile-treated sample. The corresponding topography images are shown in Figure S12 (Supporting Information).

Elastic modulus maps of the pristine IDT-BT and acetonitrile-treated films were recorded (Figure 4b,e) to gain further insight into the morphology of the different regions in the films. The reference film has a more uniform elastic modulus distribution with a single Gaussian distribution fitted to the modulus histograms and an average of 1.4 ± 0.35 GPa (Figure 4c). This modulus value is in good agreement with a previously measured value of 1.2 GPa for a time-stabilized IDT-BT sample.[43] In comparison, we find a bimodal distribution with softer and stiffer areas for the acetonitrile-treated films, as clearly observed in Figure 4f,i for 1 µm × 1 µm and 0.5 µm × 0.5 µm areas. By fitting the distribution to two Gaussians, we extracted average modulus values for the stiffer and softer areas of 1.6 ± 0.7 GPa and 0.63 ± 0.31 GPa for 1 µm × 1 µm scans, and 1.5 ± 0.6 GPa and 0.7 ± 0.2 GPa for 0.5 µm × 0.5 µm scans, respectively. The

© 2023 The Authors. Advanced Materials published by Wiley-VCH GmbH

15214095, 2023, 16, Downloaded from https://onlinelibrary.wiley.com/doi/10.1002/adma.202205377 by MPI 355 Polymer Research, Wiley Online Library on [10/07/2023]. See the Terms and Conditions (https://onlinelibrary.wiley.com/terms-and-conditions) on Wiley Online Library for rules of use; OA articles are governed by the applicable Creative Commons License

15214095, 2023, 16, Downloaded from https://onlinelibrary.wiley.com/doi/10.1002/adma.202205377 by MPI 355 Polymer Research, Wiley Online Library on [10/07/2023]. See the Terms and Conditions (https://onlinelibrary.wiley.com/terms-and-conditions) on Wiley Online Library for rules of use; OA articles are governed by the applicable Creative Commons License

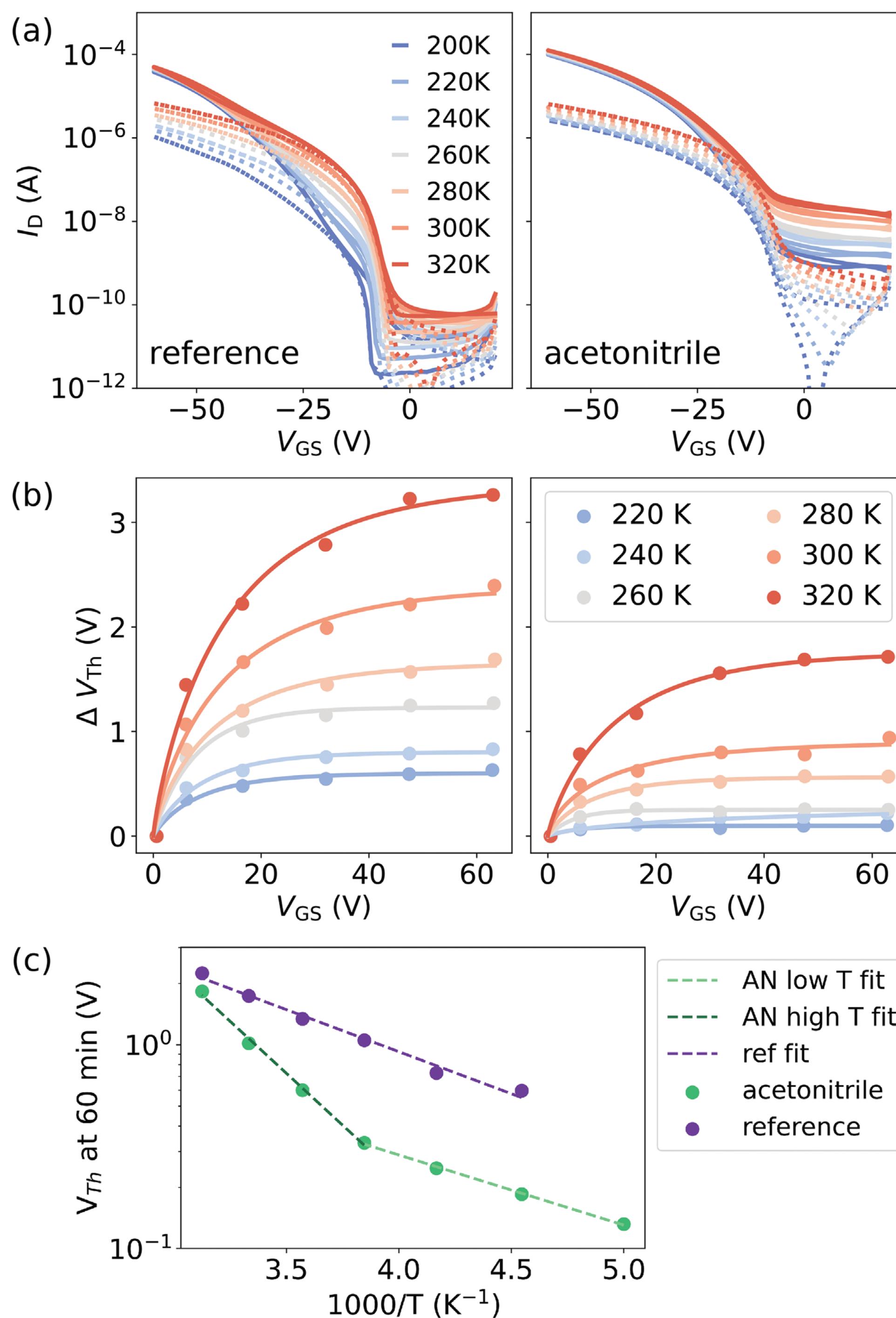

Figure 3. Low-temperature measurements of the acetonitrile-treated and the reference devices between 200 and 320 K. a) Transfer curves of the reference (left panel) and the acetonitrile-treated sample (right panel) in saturation (solid lines) and linear (dashed lines) regimes at the given temperatures. b) Threshold-voltage shift (points) of the reference (left panel) and the acetonitrile-treated device (right panel) under OFF-state bias stress at $V_{GS} = 50$ and $V_{DS} = -5$ V. The stretched exponential fit is shown as a solid line. c) Voltage-threshold shift extracted at 60 min from the stretched exponential fit from (b) against 1000/T (dots) and a linear fit (dotted lines).

bimodal distribution contains a tail of high modulus values up to 3.5 GPa in the antisolvent-treated samples suggesting that the treatment induces regions of higher modulus. The peaks in the topographic scans correspond to higher modulus values, which indicate that stiffer regions might be associated with aggregation/crystallization.

We further examined the influence of the treatment on the ordering of the polymer chains by performing grazing-incidence

© 2023 The Authors. Advanced Materials published by Wiley-VCH GmbH

15214095, 2023, 16, Downloaded from https://onlinelibrary.wiley.com/doi/10.1002/adma.202205377 by MPI 355 Polymer Research, Wiley Online Library on [10/07/2023]. See the Terms and Conditions (https://onlinelibrary.wiley.com/terms-and-conditions) on Wiley Online Library for rules of use; OA articles are governed by the applicable Creative Commons License

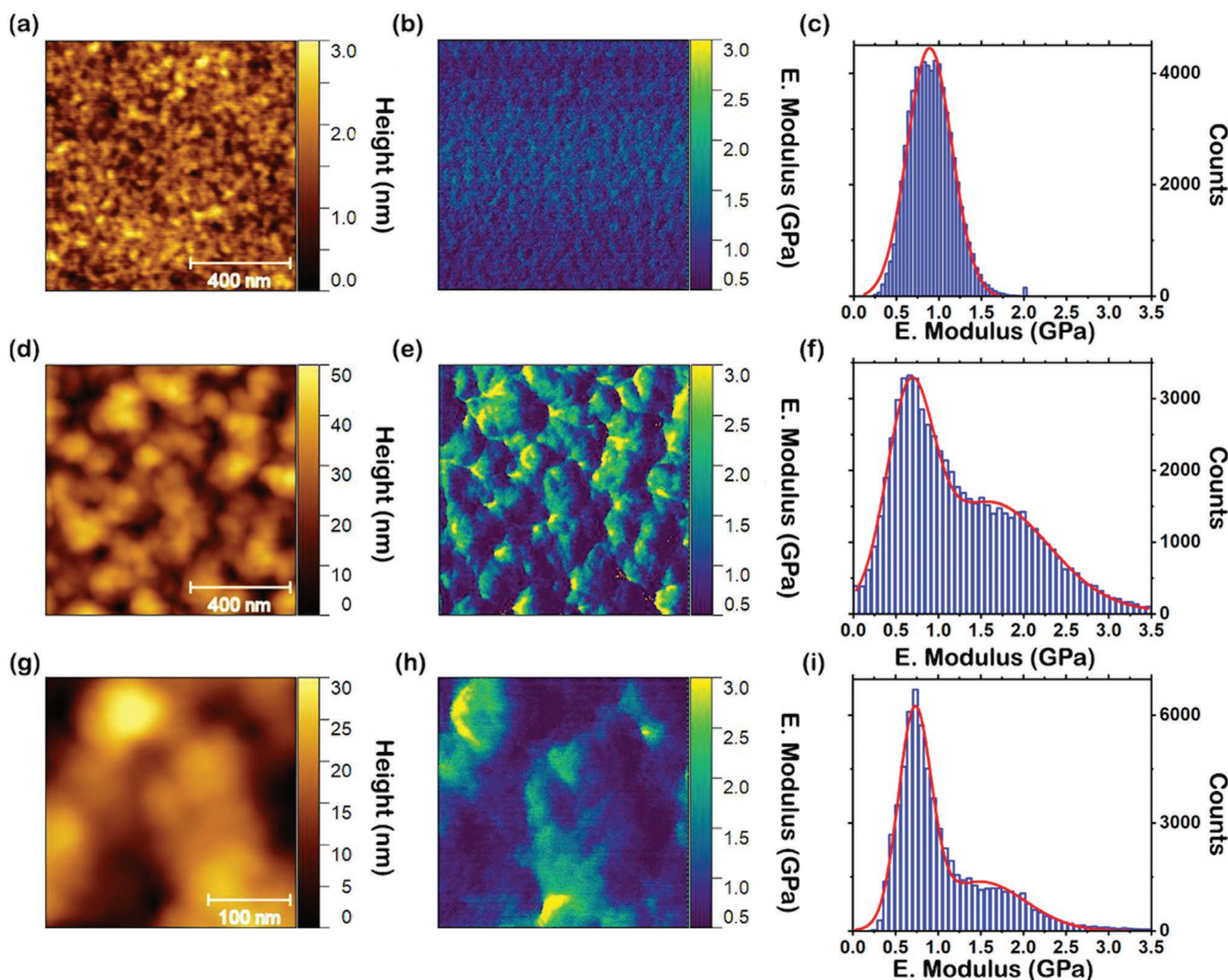

Figure 4. a,d,g) ImAFM topography of the pristine IDT-BT film (a) and films treated with acetonitrile (d,g). b,e,h) The corresponding evaluated elastic modulus maps. c,f,i) Histograms demonstrating modulus distribution, where Gaussian fit peaks are shown as red lines. The AFM scans were measured over an area of 1 µm × 1 µm of the pristine (a–c) and the acetonitrile-treated (d–f) samples, and also 0.5 µm × 0.5 µm (g–i) for the latter.

wide-angle X-ray scattering (GIWAXS) measurements on 60 nm-thick IDT-BT film deposited on silicon (**Figure 5**a,b). Consistent with previous GIWAXS measurements on IDT-BT,[44] both the reference and the treated samples exhibited weakly crystalline features as indicated by an isotropic scattering halo at $q \approx 1.2$ Å^{-1} originating from the amorphous domain in the film, a broad crystalline (010) π–π stacking peak at $q \approx 1.5$ Å^{-1}, and a crystalline (100) lamellar stacking peak with only one order of reflection at $q \approx 0.26$ Å^{-1}. The observation of the broad π–π stacking and lamellar stacking peaks in the out-of-plane direction indicates the coexistence of both face-on and edge-on oriented small crystallites. The weaker crystalline peaks oriented in-plane were indexed to (00*l*) reflections, corresponding to structural order along the polymer backbone. Both samples showed similar peak positions, suggesting a negligible change in crystallographic distances upon antisolvent treatment.

Although the GIWAXS data of both samples are broadly similar, a detailed analysis revealed subtle but important differences. The treated sample exhibited a narrower out-of-plane lamellar stacking peak along with a broader intensity distribution across the azimuthal direction (Figure 5c,d), indicating a longer coherence length, L_c (L_c = 68.6 and 93.9 Å in the reference and treated samples, respectively), but with crystallites adopting a wider orientation distribution with respect to the substrate normal. Moreover, it showed a higher relative degree of crystallinity as reflected by a 3 times higher ratio of (100) to the amorphous peak area and a 2.2 times higher ratio of (001) to the amorphous peak area (Figure 5e). We attribute these results to the introduction of the orthogonal solvent to a wet film of IDT-BT that promotes crystallization and aggregation of the film. This picture is consistent with the intermodulation AFM measurements showing the formation of aggregated regions with a higher modulus.

We also performed variable angle spectroscopic ellipsometry (VASE) and found evidence for an enhanced void fraction in the acetonitrile-treated films compared to the reference samples (Section S3, Supporting Information). This is potentially consistent with the enhanced crystallization and aggregate formation in the treated films found by ImAFM and GIWAXS, as crystallization is likely to manifest itself in ellipsometry as

© 2023 The Authors. Advanced Materials published by Wiley-VCH GmbH

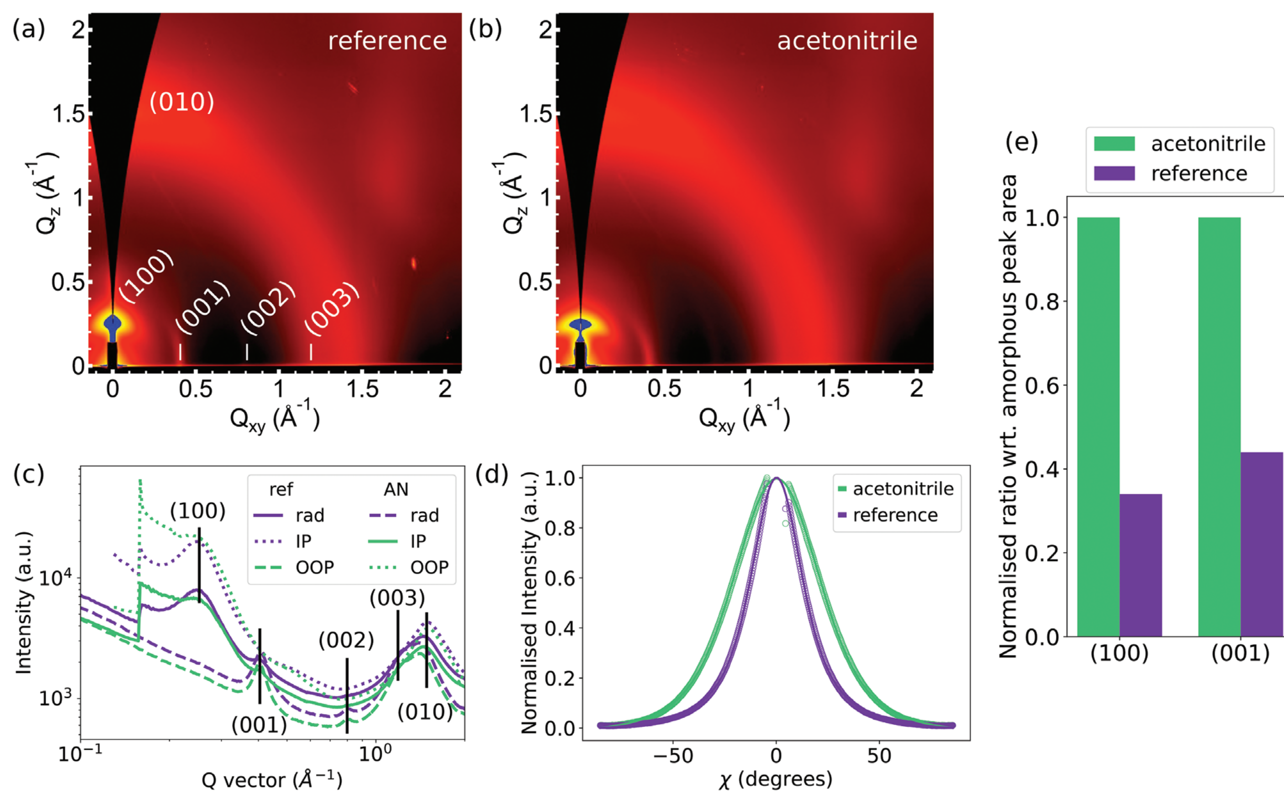

Figure 5. Microstructure of the pristine IDT-BT film and after treatment with acetonitrile. a,b) 2D GIWAXS patterns of pristine (a) and acetonitrile-treated (b) films. c) Radial (rad), in-plane (IP), and out-of-plane (OOP) 1D GIWAXS profiles. d) Normalized pole figure along $q = 0.25$ Å^{-1} for the two samples. e) Normalized ratio of the crystalline (100) and (001) peaks with respect to the amorphous peak area.

regions with higher chain density surrounded by regions of lower chain density.[45]

5. Environmental Stability

What is remarkable about the effects of the antisolvent treatment of OFETs is that it improves not just performance and OFF-state stress stability but also other metrics that are relevant for device applications. As shown in Figure S14 (Supporting Information), we observe improved stability when the devices are stored in N_2 for up to 40 days, with threshold voltage decreasing by only 8 V and the ON current by 20% compared to 15 V and 60% for the reference. Antisolvent treatment also provides superior air stability, as depicted in **Figure 6**a. We observe close to no change in the transfer curve when the acetonitrile-treated device is exposed to air for a total of 90 min, whereas in the reference device, a significant change is seen as early as after 30 min of exposure with a threshold-voltage shift of 1 V and a 20% drop in saturation mobility. This shift is often attributed to oxygen doping of organic semiconductors,[46] where an electron transfer from the polymer to oxygen occurs, leading to extra hole formation under no externally applied bias and an increase of ON and OFF currents. We also show that the anti-solvent-treated device is more stable in air and exhibits a better OFF-state bias-stress response after air exposure, as illustrated in Figure 6b. This result demonstrates that the antisolvent treatment retains its OFF-state bias-stress stability improving effect even after air exposure. We further conclude that the antisolvent-induced improvements are not primarily caused by oxygen impurities that could be present in the polar antisolvent and become incorporated into the films during the treatment. If this was the case, the reference devices would be expected to show improved OFF state bias stress stability after air exposure.

Finally, we investigated the influence of illumination on the OFF-state bias-stress stability. Nasrallah et al. showed that diF-TES ADT exhibits more pronounced instabilities and a slower recovery when a device is exposed to light compared to the dark condition.[25] We observe the same effect in pristine IDT-BT devices as 1.5 times increase in V_{Th} shift after illumination. The antisolvent treatment efficiently suppresses the additional light-induced V_{Th} shift instabilities resulting in only a negligible difference between the high and the low illumination, as seen in Figure 6c. In contrast, we do not observe any trends in the mobility change upon illumination. This result suggests that the devices that underwent the antisolvent treatment are less sensitive to the light-induced electron-trapping processes that cause the increased V_{Th} upon illumination.

6. Results and Discussion

We now discuss a potential mechanism for enhancing OFF-state bias-stress stability induced by the antisolvent treatment consistent with the above experimental observations. We emphasize that the effect is unlikely to be caused by residual

© 2023 The Authors. Advanced Materials published by Wiley-VCH GmbH

15214095, 2023, 16, Downloaded from https://onlinelibrary.wiley.com/doi/10.1002/adma.202205377 by MPI 355 Polymer Research, Wiley Online Library on [10/07/2023]. See the Terms and Conditions (https://onlinelibrary.wiley.com/terms-and-conditions) on Wiley Online Library for rules of use; OA articles are governed by the applicable Creative Commons License

15214095, 2023, 16, Downloaded from https://onlinelibrary.wiley.com/doi/10.1002/adma.202205377 by MPI 355 Polymer Research, Wiley Online Library on [10/07/2023]. See the Terms and Conditions (https://onlinelibrary.wiley.com/terms-and-conditions) on Wiley Online Library for rules of use; OA articles are governed by the applicable Creative Commons License

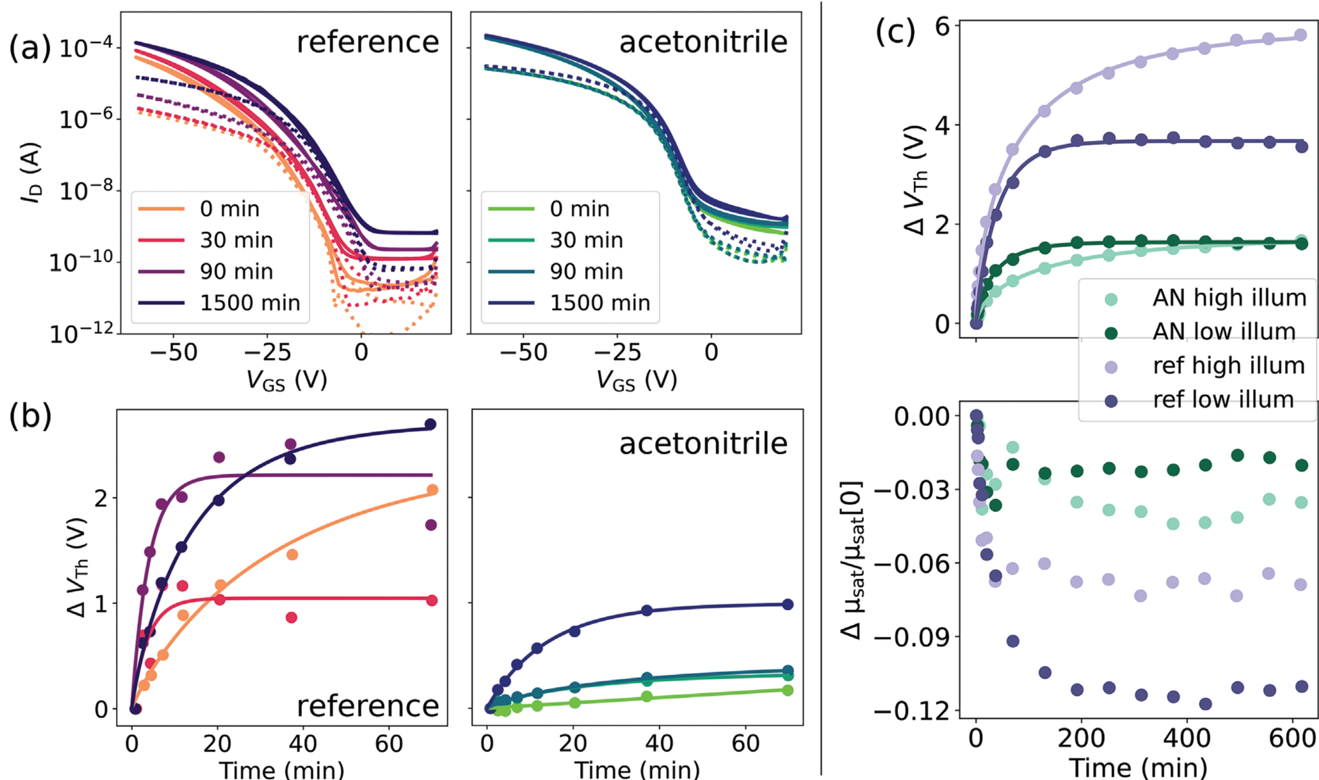

Figure 6. Air stability and OFF-state bias-stress stability (under $V_{DS} = -5$ and $V_{GS} = 50$ V) of the devices under various environmental conditions. a) Transfer curves and b) threshold-voltage shift under OFF-state-bias stress measured in N_2 of pristine IDT-BT (left) and acetonitrile-treated (right) devices after exposure to air for a given amount of time. c) Threshold-voltage shift (top) and change in saturation mobility (bottom) under high and low illumination with OFF-state-bias stress applied to reference (ref) and acetonitrile-treated (AN) devices.

antisolvent in the films. Not only do we anneal the films at a temperature significantly above the boiling point of the antisolvents, but we also observe the beneficial effect of the treatment to be retained for periods longer than one month after device fabrication (Figure S14, Supporting Information). In the literature, solvent-assisted improvement of the transfer characteristics has been attributed to removing water-related traps through the expulsion of water from the film by azeotrope formation and dry annealing.[33] This approach can be further improved using solvent-vapor annealing to cause film densification and prevent water re-uptake.[47] A similar treatment of solvent-assisted re-annealing has been shown to preferentially dissolve disordered polymer regions allowing for improvement of the packing order in the polymer films.[48] In our experiments, the emergence of the high-modulus tail in the distribution of the AFM nanomechanical mapping and the evidence from GIWAXS measurements for a higher degree of crystallinity and longer coherence length in the treated films than in the untreated films show that the antisolvent treatment has a similar effect. The treatment leads to subtle changes in the diffraction pattern that provide evidence for enhanced crystallite formation in the otherwise weakly crystalline IDT-BT films. As discussed above the antisolvent treatment is only effective when it is applied while the good solvent from which the polymer is deposited still remains in the film. This suggests that the effect involves swelling of the wet polymer film with a poor solvent, which is then likely to lead to enhanced aggregation and crystallization.

It has been argued previously that the presence of crystallites with close π–π stacking within the semicrystalline polymer microstructure is essential to achieving high carrier mobilities.[49] Weakly crystalline systems, such as IDT-BT, show that this can be fulfilled even if the crystallites are very small,[50] as long as other requirements for high mobility charge transport are met. In particular, it is important to ensure a low degree of energetic disorder along the polymer backbone. This is achieved in conformations with high barriers to torsion, and results in more efficient charge transport along the tie chains between small crystallites.[28] While it was previously thought that the small crystallites present in pristine samples of IDT-BT are sufficient to support high charge-carrier mobilities of >1 $cm^2\ V^{-1}\ s^{-1}$, our results suggest that both stability and performance benefit from the formation of slightly larger crystallites than those present in pristine IDT-BT films processed from good solvents.

In relation to the improved OFF-state bias-stress stability, threshold-voltage shifts to more positive values under OFF-state conditions are generally attributed to deep trap states for electrons.[51] They can be injected into the semiconducting channel under depletion stress conditions, even if high work function contacts are used.[52] OFF-state stability in *p*-type materials with electron affinities of <4 eV is widely attributed to the trapping

 © 2023 The Authors. Advanced Materials published by Wiley-VCH GmbH

15214095, 2023, 16, Downloaded from https://onlinelibrary.wiley.com/doi/10.1002/adma.202205377 by MPI 355 Polymer Research, Wiley Online Library on [10/07/2023]. See the Terms and Conditions (https://onlinelibrary.wiley.com/terms-and-conditions) on Wiley Online Library for rules of use; OA articles are governed by the applicable Creative Commons License

of these electrons by impurities such as water/O_2 complexes.[53] These trapped negative charges facilitate the formation of a hole accumulation layer and cause a positive threshold-voltage shift that persists until the trapped electrons recombine with injected holes. Light can further enhance this process.[13]

Electrons moving through the network of polymer chains under OFF-state conditions are likely to spend significant time in the crystallites near the sites where the interchain transfer occurs. Therefore, they may be particularly sensitive to electron-trapping impurities incorporated close to these sites. Larger aggregates/crystallites, induced by the antisolvent treatment, reduce the probability that water/O_2 complexes become incorporated in the vicinity of these sites, hence, the likelihood of electron trapping under OFF-state conditions is lower. This explanation for the improved OFF-state stress stability is entirely consistent with the associated changes in thin-film microstructure.

The formation of larger and better-ordered crystallites could also be responsible for the improved ON-state characteristics, steeper subthreshold slopes and reduced hole trap formation in antisolvent treated films. Not only the transport of electrons but also that of holes is sensitive to the local environment encountered in the vicinity of the sites where interchain hopping occurs. Hole traps may be caused by the paracrystalline disorder in the π–π stacking[49] or by the presence of impurities, such as highly polarizable water molecules.[22,47] Larger crystallites make it less likely that such impurities become incorporated close to the interchain hopping sites.

An alternative explanation for the improved ON-state characteristics is a p-doping effect associated with unintentional oxygen exposure, which is known to be beneficial for ON-state performance of polymers such as IDT-BT.[22] It is responsible for the changes in the characteristics of pristine devices upon exposure to air (Figure 6a). A small concentration of residual O_2 may be dissolved in the polar antisolvent leading to *p*-doping and filling of shallow hole traps. Although we perform the antisolvent treatment in a nitrogen atmosphere using anhydrous solvents, we cannot fully exclude this. However, we have seen no difference in the effectiveness of the antisolvent treatment when we de-oxygenate the antisolvent before use by bubbling nitrogen gas through the solution. We would like to emphasize that, even if such a mechanism plays a role in the ON-state characteristics, it is unlikely to be responsible for the improved OFF-state stability discussed above since the beneficial effect of the anti-solvent treatment is retained after exposure of the devices in the air (Figure 6b).

7. Conclusion

We report a novel approach to enhancing the performance as well as environmental and OFF-state-bias-stress stability of OFETs with weakly crystalline, high-mobility conjugated polymers using an antisolvent treatment. The improved OFF-state bias-stress stability was linked to polymer aggregation and increased crystallinity, reducing the likelihood of electron-trapping impurities becoming incorporated near the sites where interchain hopping occurs. Our work highlights the importance of the presence of crystalline aggregates even in high-performance disorder-free polymers, in which efficient charge transport and high charge-carrier mobilities had been believed to be achievable by relying simply on a network of close-contact points between adjacent polymer chains, but not requiring larger crystalline aggregates. Here, we demonstrate that to achieve sufficient bias-stress stability in these polymers the formation of larger crystalline aggregates is in fact desirable. Our results introduce an effective general strategy for improving the performance and OFF-state stress stability of high-mobility weakly crystalline conjugated polymers that involves enhancing the aggregation of the polymer chains in the vicinity of the close-crossing points.

8. Experimental Section

Materials: C16-IDT-BT (poly(indaceno(1,2-b:5,6-b′)dithiophene-*co*-2,1,3-benzothiadiazole); (M_w = 316.8 kDa, PDI 2.8) and DPP-BTz (poly((2,5-bis(2-octadecyl)- 2,3,5,6-tetrahydro-3,6-diketopyrrolo(3,4-c)pyrrole-1,4-diyl)-*alt*-(2-oc-tylnonyl)-2,1,3-benzotriazole); M_w = 63 kDa, PDI = 3.2) were synthesized according to the previous literature.[54,55] Cytop M-grade (CTL-809M) was purchased from AGC Inc. Anhydrous acetonitrile (assay >99.9%, water <0.0010%, residue <0.0001%) and *n*-butyl acetate (assay >99.7%, water <0.0025%, residue <0.0001%) were purchased from Romil.

Device Fabrication: Top-gate bottom-contact FETs were fabricated on Corning Eagle XG, 0.7 mm-thick-glass 15 mm × 15 mm substrates that were washed by sonication in DI water, acetone, and IPA for 10 min each, followed by a plasma treatment at 300 W for 10 min. The substrates were subjected to a positive photolithography process and evaporation of 4/20 nm of Ti/Au yielding a pattern of interdigitated electrodes with W = 1000 µm and L = 20 µm.

The electrodes were plasma treated at 300 W for 10 min and then transferred to a nitrogen glovebox before spin-coating IDT-BT (DPP-BTz) from 10 g L^{-1} solution in DCB that was preheated at 60 °C (110 °C) for at least 1 h. The films were spun at 500 rpm for 3 s, followed by a fast step of 1500 rpm for 60 s to yield ≈60 nm thick films. IDT-BT films were annealed at a preheated hotplate for 60 min at 90 °C, whereas DPP-BTz films were annealed for 60 mins at 110 °C. The Cytop dielectric was spun at 500 rpm for 2 s followed by 2000 rpm for 20 s and annealed at 90 °C for 20 min to yield ≈500 nm films. All the film processing was performed inside an MBraun LabMaster 130 glovebox.

This was followed by a shadow mask evaporation of 30 nm Al, with the first 5 nm evaporated slowly at 0.2–0.3 Å s^{-1}, and then 25 nm evaporated at 1 Å s^{-1}.

The devices were exposed to air for <5 min before and after gate evaporation. They were then moved to a Belle Ltd glovebox (<5 ppm O_2, <10 ppm H_2O) for storage and measurements.

Antisolvent Treatment: For the antisolvent treatment, the IDT-BT films were left on the spin-coater chuck after film deposition, and 200 µL of the antisolvent (acetonitrile or *n*-butyl acetate) were deposited straight away on the wet film to cover the whole substrate. After 2 min, the antisolvent was spun away at 1500 rpm for 60 s, and the films were annealed at 90 °C for 60 min. To avoid the absorption of antisolvent vapors into the reference samples, the glovebox was purged during fabrication, and the reference samples were kept away from the spin-coater.

FET Measurements and OFF-State Bias-Stress Procedure: All the FET and stress characteristics were measured using Agilent 4155B SPA under N_2 conditions. A forward and reverse sweeps between V_{GS} = 20 and –60 V at V_{DS} = –5 V for the linear regime and V_{DS} = –60 V for the saturation regime were measured for the transfer characteristics of the OFETs. The forward and reverse output characteristics were measured between V_{DS} = 0 and –60 V at V_{GS} = 0 to –60 V with –10 V steps.

To measure the OFF-state bias-stress stability of the devices, they were subjected to continuous stress of V_{GS} = 50 V and V_{DS} = –5 V. Before the application of stress, transfer and output characteristics of the device were

© 2023 The Authors. Advanced Materials published by Wiley-VCH GmbH

15214095, 2023, 16, Downloaded from https://onlinelibrary.wiley.com/doi/10.1002/adma.202205377 by MPI 355 Polymer Research, Wiley Online Library on [10/07/2023]. See the Terms and Conditions (https://onlinelibrary.wiley.com/terms-and-conditions) on Wiley Online Library for rules of use; OA articles are governed by the applicable Creative Commons License

measured. Then, the stress was interrupted for ≈20 s at a time to take transfer-curve measurements with a short integration time to avoid de-trapping of charges. To measure the recovery profile, the bias was removed from the devices, and their transfer characteristics were measured periodically.

Low-Temperature OFF-State Bias-Stress Procedure: The low-temperature OFF-state bias stability was measured using Agilent 4155C SPA under the pressure of 10^{-5} mbar. The samples were first cooled down to 200 K, and the OFF-state-stress measurement procedure was applied after 30 min of thermal equilibration of the stage with the samples. This sequence was repeated upon heating with 20 K intervals up to 320 K. Thanks to the experiment design, the samples were kept unbiased for at least 2 h between the consecutive OFF-state bias measurements, allowing the devices to recover between the measurements.

Environmental Stability Measurements: For the light-stability measurements, the reference devices (low illumination) were biased under room illumination with the microscope light turned off (as per standard OFF-state-bias measurement). The devices under high illumination were biased under the light microscope with the light power source set to the same value.

For the air exposure measurements, first, the regular OFF-state-bias stress procedure would be applied under N_2 conditions. Then, the samples would be exposed to air for a given amount of time, and the OFF-state-bias stress measurement would be performed again under N_2.

Parameter Extraction: Threshold-voltage shift was extracted by applying a linear regression fit to the $\sqrt{I_D}$ versus V_{GS} saturation plot in the region between −60 and −50 V.

Linear charge-carrier mobility was determined from the slope of I_D versus V_{GS}, evaluated at $V_{DS} = -5$ V, following the equation:

$$\mu_{lin} = \frac{L}{WC_i V_{DS}} \frac{\partial I_D}{\partial V_{GS}} \tag{1}$$

Whereas saturation charge-carrier mobility was determined from the slope of $\sqrt{I_D}$ versus V_{GS}, following the equation:

$$\mu_{sat} = \frac{2L}{WC_i} \left(\frac{\partial \sqrt{I_D}}{\partial V_{GS}} \right)^2 \tag{2}$$

Where W is the width of the device, L is the length of the device, and C_i is the capacitance of the 500 nm-thick Cytop dielectric layer.

Subthreshold swing was determined by fitting the following equation between the threshold and the onset voltages.

$$S = \frac{\partial V_{GS}}{\partial \log(I_D)} \tag{3}$$

Grazing-Incidence Wide-Angle X-ray Scattering: GIWAXS measurements were performed at the SAXS/WAXS beamline at the Australian Synchrotron, with the samples prepared one week before.[56] 15.2 keV photons were used as the X-ray source, and the 2D scattering patterns were recorded using an in-vacuum Dectris Pilatus 2M detector placed ≈63 cm downstream from the sample. The entire beam path was under vacuum to minimize diffuse scattering from air to improve the signal-to-noise ratio. The scattering patterns were measured as a function of incident angle. The data shown were acquired with an angle of incidence near the critical angle that maximized scattering intensity from the sample. A new spot was used for each measurement to minimize X-ray-induced damage. The total exposure time was 3 s, with the reported scattering patterns being a composite of three separate 1 s exposures taken with different detector positions to fill in the regions missed by gaps on the detector. The sample-to-detector distance was calibrated using a silver behenate standard. Data reduction and analysis were performed using an altered version of the NIKA analysis package implemented in Igor.[57]

Variable-Angle Spectroscopic Ellipsometry: VASE was measured using an M2000 ellipsometer (Woollam Co.) and angles of incidence between 40° and 70° and a wavelength range from 1700 to 400 nm. The data were fitted using the Maxwell–Garnett model that describes the film as a mixture of a material with optical constants of IDT-BT and spherical inclusions of a transparent material with refractive index n and fraction f_{void} relative to the film material.

Intermodulation AFM: The intermodulation atomic force microscopy (ImAFM) measurements were conducted using a Bruker Dimension Icon AFM connected to a multi-frequency lock-in amplifier (MLA, Intermodulation Products AB, Sweden). MLA was used to generate the drive signals and record the intermodulation data, which was further analyzed using the IMP software suite (Intermodulation Products AB) and Gwyddion (v2.59). The scan rate for the ImAFM measurements was 1.57 Hz, and the recorded images contain 256 × 256 data points. Tap300DLC probe with a diamond-like carbon tip coating of nominal spring constant of 40 N m^{-1} was used. The actual probe spring constant was calibrated using the in-built thermal calibration method before the measurements. The outer radius of the tip was evaluated to be ≈9–10 nm before and after the measurements by comparison with a sample of known elastic modulus (polystyrene PSFILM-12M, Bruker). All experiments were performed in ambient air. The elastic modulus data were generated by applying Amplitude Dependent Force Spectroscopy (ADFS) method, which extracts the in-phase (elastic) and out-of-phase (viscous) contributions to tip-surface interactions and reconstructs the nonlinear tip-surface force.[58]

Supporting Information

Supporting Information is available from the Wiley Online Library or from the author.

Acknowledgements

The authors acknowledge funding from the Engineering and Physical Sciences Research Council (EPSRC, EP/R031894/1). D.S. acknowledges support from the EPSRC Centre for Doctoral Training (CDT) in Sensor Technologies and Application (EP/L015889/1). H.U. acknowledges funding from EPSRC (EP/S030662/1). M.N. acknowledges Ph.D. studentship support from FlexEnable Ltd.

Note: The article number for ref. [2] was corrected on April 20, 2023, after initial publication online.

Conflict of Interest

H.S. is a co-founder of FlexEnable Ltd.

Data Availability Statement

The data that support the findings of this study are available from the corresponding author upon reasonable request.

Keywords

bias-stress effects, electron trapping, organic field-effect transistors, solvent treatments, stability

Received: June 14, 2022
Revised: October 10, 2022
Published online: March 10, 2023

[1] X. Liu, Y. Guo, Y. Ma, H. Chen, Z. Mao, H. Wang, G. Yu, Y. Liu, *Adv. Mater.* **2014**, *26*, 3631.
[2] J. Li, Y. Zhao, H. S. Tan, Y. Guo, C. A. Di, G. Yu, Y. Liu, M. Lin, S. H. Lim, Y. Zhou, H. Su, B. S. Ong, *Sci. Rep.* **2012**, *2*, 754.
[3] H. Iino, T. Usui, J. I. Hanna, *Nat. Commun.* **2015**, *6*, 6828.

© 2023 The Authors. Advanced Materials published by Wiley-VCH GmbH

[4] H. Chang, W. Li, H. Tian, Y. Geng, H. Wang, D. Yan, T. Wang, *Org. Electron.* **2015**, *20*, 43.
[5] S. Park, S. H. Kim, H. H. Choi, B. Kang, K. Cho, *Adv. Funct. Mater.* **2020**, *30*, 1904590.
[6] J. Liang, E. A. Schiff, S. Guha, B. Yan, J. Yang, *Appl. Phys. Lett.* **2006**, *88*, 063512.
[7] H. F. Haneef, A. M. Zeidell, O. D. Jurchescu, *J. Mater. Chem. C* **2020**, *8*, 759.
[8] H. Sirringhaus, *Adv. Mater.* **2014**, *26*, 1319.
[9] H. Bronstein, C. B. Nielsen, B. C. Schroeder, I. McCulloch, *Nat. Rev. Chem.* **2020**, *4*, 66.
[10] W. H. Lee, H. H. Choi, D. H. Kim, K. Cho, *Adv. Mater.* **2014**, *26*, 1660.
[11] X. Jia, *Sci. Adv.* **2018**, *8*, 1501591.
[12] S. Y. Son, Y. Kim, J. Lee, G. Y. Lee, W. T. Park, Y. Y. Noh, C. E. Park, T. Park, *J. Am. Chem. Soc.* **2016**, *138*, 8096.
[13] H. Lee, B. Moon, S. Y. Son, T. Park, B. Kang, K. Cho, *ACS Appl. Mater. Interfaces* **2021**, *13*, 16722.
[14] C. Yumusak, N. S. Sariciftci, M. Irimia-Vladu, *Mater. Chem. Front.* **2020**, *4*, 3678.
[15] M. Kettner, M. Zhou, J. Brill, P. W. M. Blom, R. T. Weitz, *ACS Appl. Mater. Interfaces* **2018**, *10*, 35449.
[16] C. Goldmann, D. J. Gundlach, B. Batlogg, *Appl. Phys. Lett.* **2006**, *88*, 2004.
[17] K. P. Pernstich, D. Oberhoff, C. Goldmann, B. Batlogg, *Appl. Phys. Lett.* **2006**, *89*, 213509.
[18] S. G. J. Mathijssen, M. J. Spijkman, A. M. Andringa, P. A. Van Hal, I. McCulloch, M. Kemerink, R. A. J. Janssen, D. M. De Leeuw, *Adv. Mater.* **2010**, *22*, 5105.
[19] J. Kim, M. Jang, T. K. An, S. Kim, H. Kim, S. H. Kim, H. Yang, C. E. Park, *Org. Electron.* **2015**, *17*, 87.
[20] B. Lee, A. Wan, D. Mastrogiovanni, J. E. Anthony, E. Garfunkel, V. Podzorov, *Phys. Rev. B: Condens. Matter. Mater. Phys.* **2010**, *82*, 085302.
[21] A. Sharma, S. G. J. Mathijssen, T. Cramer, M. Kemerink, D. M. De Leeuw, P. A. Bobbert, *Appl. Phys. Lett.* **2010**, *96*, 103306.
[22] M. Nikolka, I. Nasrallah, B. Rose, M. K. Ravva, K. Broch, A. Sadhanala, D. Harkin, J. Charmet, M. Hurhangee, A. Brown, S. Illig, P. Too, J. Jongman, I. McCulloch, J. L. Bredas, H. Sirringhaus, *Nat. Mater.* **2017**, *16*, 356.
[23] M. P. Hein, A. A. Zakhidov, B. Lüssem, J. Jankowski, M. L. Tietze, M. K. Riede, K. Leo, *Appl. Phys. Lett.* **2014**, *104*, 013507.
[24] H. Phan, M. J. Ford, A. T. Lill, M. Wang, G. C. Bazan, T. Q. Nguyen, *Adv. Funct. Mater.* **2017**, *27*, 1701358.
[25] I. Nasrallah, M. K. Ravva, K. Broch, J. Novak, J. Armitage, G. Schweicher, A. Sadhanala, J. E. Anthony, J. L. Bredas, H. Sirringhaus, *Adv. Electron. Mater.* **2020**, *6*, 2000250.
[26] J. Smith, R. Hamilton, I. McCulloch, N. Stingelin-Stutzmann, M. Heeney, D. D. C. Bradley, T. D. Anthopoulos, *J. Mater. Chem.* **2010**, *20*, 2562.
[27] X. Zhang, H. Bronstein, A. J. Kronemeijer, J. Smith, Y. Kim, R. J. Kline, L. J. Richter, T. D. Anthopoulos, H. Sirringhaus, K. Song, M. Heeney, W. Zhang, I. McCulloch, D. M. Delongchamp, *Nat. Commun.* **2013**, *4*, 2238.
[28] D. Venkateshvaran, M. Nikolka, A. Sadhanala, V. Lemaur, M. Zelazny, M. Kepa, M. Hurhangee, A. J. Kronemeijer, V. Pecunia, I. Nasrallah, I. Romanov, K. Broch, I. McCulloch, D. Emin, Y. Olivier, J. Cornil, D. Beljonne, H. Sirringhaus, *Nature* **2014**, *515*, 384.
[29] R. A. Street, A. Salleo, *Appl. Phys. Lett.* **2002**, *81*, 2887.
[30] K. Bulgarevich, K. Sakamoto, T. Yasuda, T. Minari, M. Takeuchi, *Adv. Electron. Mater.* **2020**, *6*, 2000161.
[31] W. L. Kalb, T. Mathis, S. Haas, A. F. Stassen, B. Batlogg, *Appl. Phys. Lett.* **2007**, *90*, 092104.
[32] H. H. Choi, K. Cho, C. D. Frisbie, H. Sirringhaus, V. Podzorov, *Nat. Mater.* **2017**, *17*, 2.
[33] M. Nikolka, G. Schweicher, J. Armitage, I. Nasrallah, C. Jellett, Z. Guo, M. Hurhangee, A. Sadhanala, I. McCulloch, C. B. Nielsen, H. Sirringhaus, *Adv. Mater.* **2018**, *30*, 1801874.
[34] H. Opoku, B. Nketia-Yawson, E. S. Shin, Y. Y. Noh, *J. Mater. Chem. C* **2018**, *6*, 661.
[35] R. A. Street, *Hydrogenated Amorphous Silicon*, Cambridge University Press, Cambridge, UK **1991**.
[36] H. Sirringhaus, *Adv. Mater.* **2009**, *21*, 3859.
[37] U. Zschieschang, R. T. Weitz, K. Kern, H. Klauk, *Appl. Phys. A: Mater. Sci. Process.* **2009**, *95*, 139.
[38] M. Urien, G. Wantz, E. Cloutet, L. Hirsch, P. Tardy, L. Vignau, H. Cramail, J. P. Parneix, *Org. Electron.* **2007**, *8*, 727.
[39] C. B. Nielsen, M. Turbiez, I. McCulloch, *Adv. Mater.* **2013**, *25*, 1859.
[40] I. E. Jacobs, G. D'avino, V. Lemaur, Y. Lin, Y. Huang, C. Chen, T. F. Harrelson, W. Wood, L. J. Spalek, T. Mustafa, C. A. O'keefe, X. Ren, D. Simatos, D. Tjhe, M. Statz, J. W. Strzalka, J. K. Lee, I. Mcculloch, S. Fratini, D. Beljonne, H. Sirringhaus, *J. Am. Chem. Soc.* **2022**, *144*, 3005.
[41] C. Sinturel, M. Vayer, M. Morris, M. A. Hillmyer, *Macromolecules* **2013**, *46*, 5399.
[42] J. Liang, W. Zhong, L. Ying, W. Yang, J. Peng, Y. Cao, *Org. Electron.* **2015**, *27*, 1.
[43] V. Panchal, I. Dobryden, U. D. Hangen, D. Simatos, L. J. Spalek, I. E. Jacobs, G. Schweicher, P. M. Claesson, D. Venkateshvaran, *Adv. Electron. Mater.* **2022**, *8*, 2101019.
[44] M. Nikolka, K. Broch, J. Armitage, D. Hanifi, P. J. Nowack, D. Venkateshvaran, A. Sadhanala, J. Saska, M. Mascal, S. H. Jung, J. K. Lee, I. McCulloch, A. Salleo, H. Sirringhaus, *Nat. Commun.* **2019**, *10*, 2122.
[45] A. Nunns, J. Gwyther, I. Manners, *Polymer* **2013**, *54*, 1269.
[46] C. K. Lu, H. F. Meng, *Phys. Rev. B: Condens. Matter Mater. Phys.* **2007**, *75*, 235206.
[47] G. Zuo, M. Linares, T. Upreti, M. Kemerink, *Nat. Mater.* **2019**, *18*, 588.
[48] C. A. Di, K. Lu, L. Zhang, Y. Liu, Y. Guo, X. Sun, Y. Wen, G. Yu, D. Zhu, *Adv. Mater.* **2010**, *22*, 1273.
[49] R. Noriega, J. Rivnay, K. Vandewal, F. P. V. Koch, N. Stingelin, P. Smith, M. F. Toney, A. Salleo, *Nat. Mater.* **2013**, *12*, 1038.
[50] C. Cendra, L. Balhorn, W. Zhang, K. O'Hara, K. Bruening, C. J. Tassone, H.-G. Steinrück, M. Liang, M. F. Toney, I. McCulloch, M. L. Chabinyc, A. Salleo, C. J. Takacs, *ACS Macro Lett.* **2021**, *10*, 1306.
[51] C. Li, L. Duan, H. Li, Y. Qiu, *J. Phys. Chem. C* **2014**, *118*, 10651.
[52] C. Siol, C. Melzer, H. Von Seggern, *Appl. Phys. Lett.* **2008**, *93*, 133303.
[53] D. Abbaszadeh, A. Kunz, N. B. Kotadiya, A. Mondal, D. Andrienko, J. J. Michels, G. J. A. H. Wetzelaer, P. W. M. Blom, *Chem. Mater.* **2019**, *31*, 6380.
[54] M. Gruber, S. H. Jung, S. Schott, D. Venkateshvaran, A. J. Kronemeijer, J. W. Andreasen, C. R. McNeill, W. W. H. Wong, M. Shahid, M. Heeney, J. K. Lee, H. Sirringhaus, *Chem. Sci.* **2015**, *6*, 6949.
[55] W. Zhang, J. Smith, S. E. Watkins, R. Gysel, M. McGehee, A. Salleo, J. Kirkpatrick, S. Ashraf, T. Anthopoulos, M. Heeney, I. McCulloch, *J. Am. Chem. Soc.* **2010**, *132*, 11437.
[56] N. M. Kirby, S. T. Mudie, A. M. Hawley, D. J. Cookson, H. D. T. Mertens, N. Cowieson, V. Samardzic-Boban, *J. Appl. Crystallogr.* **2013**, *46*, 1670.
[57] J. Ilavsky, *J. Appl. Crystallogr.* **2012**, *45*, 324.
[58] D. Forchheimer, D. Platz, E. A. Tholén, D. B. Haviland, *Phys Rev B Condens Matter Mater Phys* **2012**, *85*, 195449.

© 2023 The Authors. Advanced Materials published by Wiley-VCH GmbH

15214095, 2023, 16, Downloaded from https://onlinelibrary.wiley.com/doi/10.1002/adma.202205377 by MPI 355 Polymer Research, Wiley Online Library on [10/07/2023]. See the Terms and Conditions (https://onlinelibrary.wiley.com/terms-and-conditions) on Wiley Online Library for rules of use; OA articles are governed by the applicable Creative Commons License